Solis Díaz, C.; Balaguer Ramirez, M.; García-Fayos, J.; Palafox, E.; Serra Alfaro, JM. (2020). Progress in Ce(0.8)Gd(0.2)O(2-delta)protective layers for improving the CO(2)stability of Ba0.5Sr0.5Co0.8Fe0.2O3-delta O2-transport membranes. Sustainable Energy & Fuels. 4(7):3747-3752. https://doi.org/10.1039/d0se00324g

ARTICLE

Progress in $Ce_{0.8}Gd_{0.2}O_{2-\delta}$ protective layers for improving the CO_2 stability of $Ba_{0.5}Sr_{0.5}Co_{0.8}Fe_{0.2}O_{3-\delta}$ O_2-transport membranes

Received 00th January 20xx,
Accepted 00th January 20xx

DOI: 10.1039/x0xx00000x

Cecilia Solís[a], María Balaguer[a], Julio Garcia-Fayos[a], Elena Palafox[a], and José M. Serra[a,*]

$Ce_{0.8}Gd_{0.2}O_{2-\delta}$ (CGO) thin films were deposited by radio frequency (RF) magnetron sputtering and temperature deposition was changed in order to optimize the microstructure and transport properties of the obtained films. Afterwards, the films were deposited on $Ba_{0.5}Sr_{0.5}Co_{0.8}Fe_{0.2}O_{3-\delta}$ (BSCF) oxygen separation membranes as CO_2 protective layers. Oxygen permeation was finally measured by sweeping both Ar and CO_2, and the obtained results compared with bare BSCF membrane. It was found that the oxygen permeation of the BSCF is improved by this CGO layer, with a 4-fold improvement in the oxygen permeation flux when using pure CO_2 as sweep gas at 900 °C. Therefore, these CGO protective layers are a promising way for overcoming the limitations of BSCF membranes under CO_2-containing environments, associated to surface competitive O_2-CO_2 adsorption and carbonation of Ba at low temperatures.

Introduction

Actual industry of fuel and chemicals relies on the syngas production as a previous step of the gas-to-liquids conversion (GTL). The mixture of hydrogen and carbon monoxide that composes the syngas can be upgraded in a second step like Fischer-Tropsch (FT) or methanol production, while hydrogen can be used in the Haber-Bosch process for ammonia synthesis. Conventional technologies for syngas production include steam reforming (SR) and autothermal reforming (AR), which are very costly, accounting for over the 50% of capital costs. Catalytic Partial Oxidation (CPO) reactors provide a more energy efficient alternative to SR and AR since it is an exothermic reaction with fast kinetics. Therefore, the process requires smaller reactor vessel and large amounts of superheated steam can be avoided. CPO consists in the substoichiometric partial combustion of fuel (coal or methane), creating a hydrogen-rich syngas through the following reactions:

$$3C + O_2 + H_2O \leftrightarrows 3CO + 2H_2 \quad (1)$$

$$CH_4 + 1/2\, O_2 \leftrightarrows \mathrm{CO} + 2H_2 \quad (2)$$

Some disadvantages are the emergence of hot spots on the catalyst due to the exothermicity of the reaction, the relatively low hydrogen production yield, the tendency to soot formation and the requirement of pure oxygen for the reaction, which can be all alleviated by the use of an oxygen transport membrane (OTM) reactor. [1]

OTM based on mixed ionic and electronic conducting (MIEC) ceramics have attracted much interest as an inexpensive alternative for industrially established cryogenic air separation.[2] OTMs present 100% selectivity, being their performance dependent on the ambipolar conductivity of the constituent material and on the operation conditions. An OTM-based membrane CPO reactor injects oxygen into the reactor in a controlled manner, in such way that the stoichiometry could be continuously adjusted, and the equilibrium of the reaction shifted to the products, enhanced by the continuous extraction of the syngas. Besides, the exothermic reaction taking place would maintain the high temperature in the membrane. [3, 4]

MIEC perovskites with the general formula $ABO_{3-\delta}$, as $SrCo_{0.8}Fe_{0.2}O_{3-\delta}$ (SCF), $Ba_{0.5}Sr_{0.5}Co_{0.8}Fe_{0.2}O_{3-\delta}$ (BSCF) and $La_{0.6}Sr_{0.4}Co_{0.2}Fe_{0.8}O_{3-\delta}$ (LSCF), are up to date the most promising candidates for OTM applications.[5-9] BSCF supported membranes have achieved up to 12.2 $ml\cdot min^{-1}\cdot cm^{-2}$ at 1000 °C under Air/Argon gradient,[9] but the main problem of these materials is their low stability in operation conditions on CO_2 containing atmospheres, which will be present to some extent in the CPO reaction. Several strategies to improve the stability against CO_2 include the doping of the perovskite structure with other transition metals like Zr or Y,[10] the combination of BSCF with a CO_2 stable material in a dual-phase composite [11, 12] (e.g. gadolinium doped ceria) or, as the goal of this work, the development of CO_2 protective layers of ionic or MIEC materials.[13,14, 15]

The material for the protective layer must fulfil several characteristics as chemical and mechanical stability in acid gas atmospheres, good ionic conductivity and thermo-structural compatibility with the protected BSCF. Among all the different predominant ionic conducting materials, doped ceria has shown very high chemical stability and can be considered as promising components for the development of stable ionic protective layer for BSCF membranes. The thermal expansion coefficient (TEC) difference of both structures (11.9×10^{-6} K^{-1} of $Ce_{0.9}Gd_{0.1}O_{2-}$

---

[a] *Address here. Instituto de Tecnología Química, Universitat Politècnica de València-Consejo Superior de Investigaciones Científicas, Avenida de los Naranjos s/n. 46022 Valencia (Spain)*

$_{\delta}$ and 19.95×10^{-6} of BSCF)[16, 17] force to use a suitable deposition technique for the ceria layer growth in order to preserve the membrane structure, avoiding cracks formation. In relation to this, Schulz et al. conducted oxygen permeation measurements on BSCF membranes spin-coated with CGO layers,[18] however the use of this technique resulted in the appearance of scattered defects in the CGO layers after sintering, and finally leading to a permeation breakdown at high CO_2 concentrations. Therefore, it is necessary the use of techniques ensuring proper layer deposition. In previous works, $NiFe_2O_4$-$Ce_{0.8}Gd_{0.2}O_{2-\delta}$ (NFO-CGO) protective layer showed the possibility of obtaining competitive oxygen flux while extending the stability of the material in CO_2 [14] Other CGO layers on LSCF made by spray pyrolysis showed a protection effect with little decrease of permeation. [13]

Aiming for the application in syngas production conditions, this work is focused on the study of the BSCF membrane stability against CO_2 when applying a thin CGO protective layer.[16, 19, 20] The CGO was deposited by RF-sputtering in order to ensure the crystallinity properties together with a small thickness, necessary for preserving the high BSCF permeation properties. First the growth of different CGO films was studied as a function of different deposition temperatures, and then the best film was grown on a BSCF bulk membrane for permeation measurements under CO_2 containing atmospheres. This CGO protective layer study will provide information to be compared with different protection layers (as composites) in terms of performance and stability.

Experimental Section

CGO powder was purchased from Treibacher Industries AG. One-inch ceramic targets were prepared by uniaxially pressing CGO into pellets at 30 kN for 3 min and subsequently sintering 5 h in air at 1400 °C. X-ray diffraction (XRD) of the sintered targets confirmed the complete formation of the corresponding fluorite structures.[21] The thin films were deposited with a Pfeiffer Classic 250 deposition system equipped with two radiofrequency (13.56 MHz) sources. The films were deposited on a rotating substrate holder, with RF power of 25 W and a target - substrate distance of 5 cm. The substrate was heated from room temperature (RT) up to 600 °C. The base pressure of the chamber before the deposition was below 2×10^{-6} mbar. The working pressure was 6.2×10^{-2} mbar with mixed argon-oxygen gas ratio 9/1. Different thicknesses were deposited and controlled by deposition duration. All samples were deposited on Si (100) and amorphous quartz substrates in order to perform different thin film characterization.

The crystal structure of the films was checked by XRD measurements carried out by a PANalytical Cubix fast diffractometer, using $CuK_{\alpha 1,2}$ radiation and an X'Celerator detector in Bragg-Brentano geometry.

The surface morphology of the films and the fracture cross sections were analyzed by ZEISS Ultra55 field emission scanning electron microscope (FESEM). The thickness of the films was determined from the fracture cross section FESEM images.

The planar electrical conductivity of the films was measured by standard four-point DC technique on films deposited on quartz substrates, by using silver wires and paste for contacting. Measurements were recorded as the temperature decreases from 800 to 400 °C at 1 °C/min at a constant atmosphere, in different oxygen partial pressures (pO_2).[16]

Oxygen permeation studies were carried out in a lab-scale quartz reactor (Fig. S1). Synthetic air (21% O_2 in the feed stream) was fed into the oxygen-rich chamber, while mixtures of argon and carbon dioxide were used as the sweep gas on the permeate side. Both streams were fed at atmospheric pressure. Inlet gases were preheated in order to ensure the correct gas temperature for contact with the membrane surface. This is particularly important when high gas flow rates are employed. All streams were individually mass flow controlled. The temperature was measured by a thermocouple attached to the membrane. A PID controller-maintained temperature variations within 2 °C of the set point. The samples consisted of gastight membranes and membrane gas leak-free conditions were achieved using gold rings heated to 970 °C for 4 h immediately prior to the measurement. The permeate was analyzed at steady state by online gas chromatography using a micro-GC Varian CP-4900 equipped with Molsieve5A, Pora-Plot-Q glass capillary, and CP-Sil modules. Membrane gas leak-free conditions were ensured by continuously monitoring the nitrogen concentration in the product gas stream. An acceptable sealing was achieved when the ratio between the oxygen leak flow and the oxygen flux was lower than 1%. The data reported here were achieved at steady state after 1 h in the reaction stream. Each GC analysis was repeated three times to minimize the analysis error. The experimental analytical error was below 0.5%.

In order to check the protective features provided by means of CGO deposition, oxygen permeation tests were performed on two BSCF membranes: one bare membrane, and the other with CGO RF sputtered coating. The membranes were obtained by uniaxially pressing BSCF powder (Fraunhofer IKTS, Germany) into pellets at 30 kN for 3 minutes and subsequently sintering in air at 1100 °C for 5 h. Thus, dense gastight membranes with a thickness of 0.8 mm were obtained. The CGO coating was deposited on the BSFC membrane by using the aforementioned RF sputtering system with a power of 25 W, and a target - substrate distance of 5 cm. The substrate temperature was 400 °C, for a deposition time of 4 h and a working pressure of 6.2×10^{-2} mbar (with mixed argon-oxygen gas ratio 9/1). Oxygen permeation tests consisted of the variation of temperature under an Air/Argon gradient in the range 950-800 °C, and the effect of varying CO_2 content in the sweep stream at 900 °C. During all the tests belonging to the membrane coated with CGO layer, synthetic air was fed into bare membrane side, whereas sweep streams (made of argon and CO_2 mixtures) were fed into CGO-protected membrane side.

Results and discussion

Figure 1 shows the XRD patterns of the obtained CGO thin films deposited at RT, 400 and 600 °C as deposited (a) and after an annealing process at 800 °C for 2 h (b). As deposited, the film grown at RT is amorphous, as indicates the absence of any diffraction peaks. When the deposition temperature is increased, the crystallization of the CGO films occurs, and the obtained films show different preferential orientations depending on the growth temperature. Thus, CGO film deposited at 400 °C shows (111) preferential orientation (deduced from the only presence of the (111) and (222) peaks).[21] When the growth temperature increases up to 600 °C the texture of the film changes to a (200) preferential orientation (although some other peaks appear). Similar temperature-dependent texture orientations were previously reported for other CGO and CeO_2 thin films obtained by different deposition techniques, although no unified explanation about (200) and (111) textures exist from theoretical and experimental points of view.[22-32] The preferential texture orientation prevails after the annealing in air at 800 °C for 2 h. The samples deposited at RT and 400 °C present the (111) orientation while the sample grown at 600 °C maintains its (200) orientation.

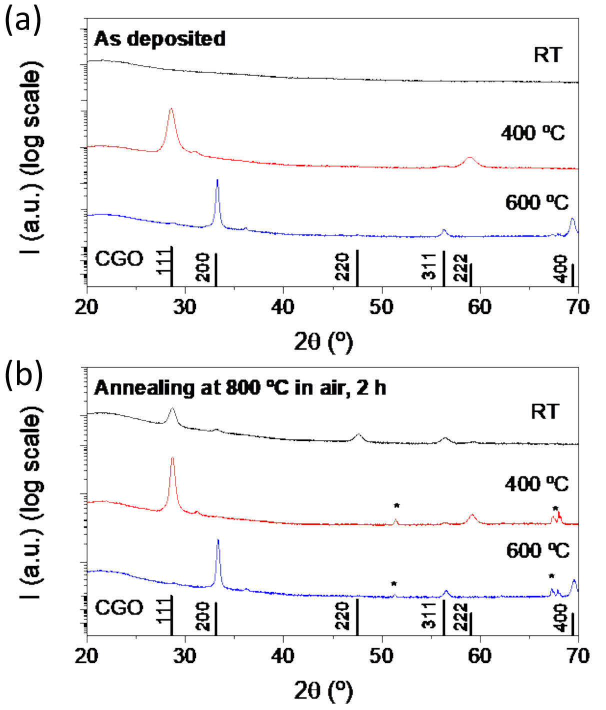

Figure 1: XRD patterns of three different CGO films deposited at RT, 400 and 800 °C (a), and after annealing in air for 2 hour at 800 °C (b), respectively. CGO reference patterns is also showed for comparison[21]. * marked peaks correspond to the XRD stainless steel holder

Surface morphology of the different CGO films grown at RT, 400 and 600 °C and the effect of the annealing at 800 °C in air for 2 h, is showed in Figure 2a-f. Films grown above RT appear crack-free and dense, independently of the deposition and post-annealing temperatures. However, films deposited at RT show some small cracks along the surface that persist after the annealing process. All the films present very small crystal sizes that make very difficult a direct comparison of the grains sizes by employing the FESEM images. Note that the cross-section images of the samples deposited at 400 and 600 °C were taken after 3 s Pt sputter deposition, thus the real grain size is difficult to calculate. Furthermore, the thickness differences showed in the samples correspond to distinct deposition times.

Conductivity properties of the CGO thin films after annealing are summarized in Figure 3. The Arrhenius behaviour of the different films is plotted together with the bulk material in Figure 3a. First of all, it should be highlighted that total conductivity of the films is up to one order of magnitude lower than that of the bulk material, as it has been previously reported for ionic conductivity in thin films compared to corresponding bulk materials.[33] Activation energy (*Ea*) of the CGO bulk material is 0.73 eV, which agrees with other reported values independently of the sintering route.[22] However, *Ea* of the CGO films is between 0.8 and 1.4 eV that agrees with reported values [26, 32, 33] In the films *Ea* slightly decreases when the deposition temperature increases from RT to 400 °C but increases when film is deposited at 600 °C (which presents different crystal orientation). This variation of *Ea* is attributed, as in other reported CGO films, to different synthesis routes and different strains that the films sustain.[33]

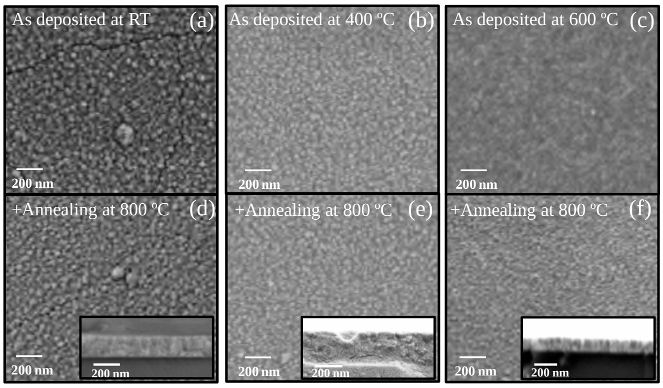

Figure 2: SEM images of different CGO films deposited at RT (a), 400 °C (b) and 800 °C (d) and after annealing in air for 2 hours at 800 °C (d), (e) and (f), respectively and corresponding cross-section images in the insets

Figure 3b shows that the conductivity of all the films is independent on the pO_2, as it corresponds to a predominant ionic conductor, regardless of the preferential crystal orientation of the material.[34, 35] Due to the best microstructure and conductivity properties of the film deposited at 400 °C, this temperature was selected for growing the protective film on the BSCF membrane and for performing the permeation measurements.

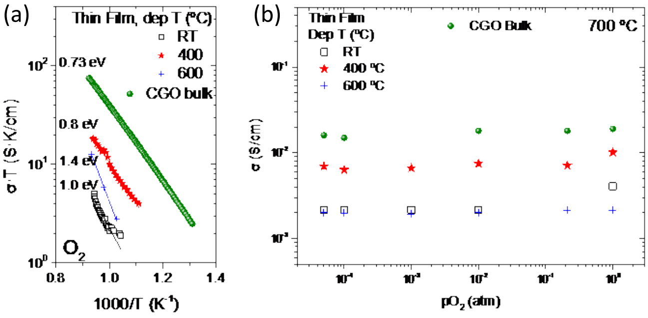

Figure 3: (a) Arrhenius diagrams for electrical conductivity of different CGO thin films and bulk material in oxygen and (b) total conductivity at 700 °C as a function of the pO_2

XRD patterns of the pristine BSCF membrane and after the deposition of a CGO sputtered film can be observed in Figure 4a, together with the CGO and BSCF reference patterns.[21, 36] All the peaks are indexed for CGO and BSCF phases, ruling out the formation of secondary phases during the coating process. Different to the layer sputtered on the SiO_2 wafer, where there is a preferential growth along the (111) direction, the layer on BSCF shows polycrystalline features. Figure 4b shows the fracture cross-section of a CGO thin film on a BSCF membrane before permeation measurements. The CGO layer is dense and covers the whole surface of the membrane. In line with XRD, the morphology of the CGO layer on BSCF is different from the layer grown on the Si wafer (sputtered at 400 °C), showing no preferential orientation as well as a good attachment to the substrate.

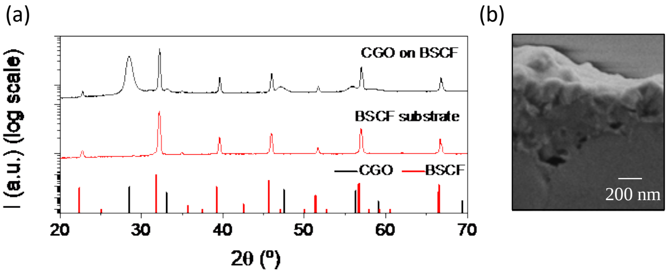

Figure 4: (a) XRD pattern of the pristine BSCF membrane and after the deposition of the CGO thin film, and CGO and BSCF reference patterns; (b) fracture cross-section of a CGO thin film on a BSCF membrane before permeation measurements.

Oxygen permeation tests were performed aiming to determine whether the addition of a CGO thin layer acts as a protection when exposed to CO_2-containing environments. Indeed BSCF membranes exhibit dramatic losses in oxyfuel-like oxygen permeation.[37-39] For that purpose, 0.8 mm-thick bare and CGO-coated BSCF membranes were studied in dependence on temperature and CO_2 content in sweep gas stream. Figure 5a shows oxygen fluxes for the abovementioned membranes when varying temperature in the range 950-800 °C under an Air/Argon gradient. This experiment was performed in order to study how CGO protective layer affects BSCF permeation behavior. The addition of a 300-500 nm CGO cover produces a slight worsening in O_2 permeation at any tested temperature range, ascribed to the lower CGO mixed conductivity that subsequently leads to lower O_2 permeation performance. Such an effect in conductivity was different to previously observed in a similar study conducted on BSCF membranes coated with a $NiFe_2O_4$-$Ce_{0.8}Gd_{0.2}O_{2-\delta}$ (NFO/CGO) layer by RF-magnetron co-sputtering[14], in which the electronic contribution of NFO improved the permeation ratios over a NFO/CGO protective layer.[40] At 950 °C, a peak O_2 flux of 5.34 ml·min^{-1}·cm^{-2} with the bare BSCF membrane is obtained, whereas oxygen permeation decreases down to 4.76 ml·min^{-1}·cm^{-2} when adding the CGO layer.

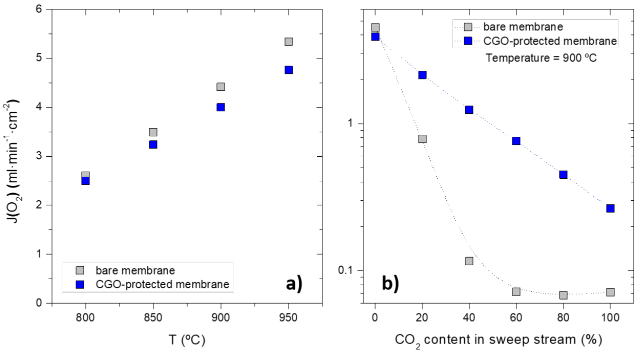

Figure 5: a) Oxygen permeation in dependence of temperature for bare and CGO-protected BSCF membranes, with the CGO film deposited at 400 ºC. Tests performed under Air/Argon gradient. Q = 300 ml·min^{-1}. b) Oxygen permeation in dependence of CO_2 content in sweep stream at 900 ºC for bare and CGO-protected BSCF membranes, with the CGO film deposited at 400 ºC. Synthetic air feeding (300 ml·min^{-1}).

O_2 permeation variation as a function of CO_2 content in sweep stream is depicted in Figure 5b for the two considered membranes. These tests were performed at 900 °C as an approach to mimic oxyfuel conditions. [41, 42] Different mixtures of Ar and CO_2 were used as sweep gases, whereas synthetic air was used as feed. As can be seen in Figure 5b, CO_2 presence in permeate side affects significantly O_2 permeation. The bare membrane suffers a dramatic loss in permeation from 4.5 down to 0.12 ml·min^{-1}·cm^{-2} with a sweep gas containing 40% CO_2, then dropping to 0.07 ml·min^{-1}·cm^{-2} O_2 at 60% CO_2 and maintaining this rate under full-CO_2 atmosphere. Similar tests on the CGO-protected membrane revealed a noteworthy lower J(O_2) worsening, since O_2 flux drops from 3.9 to 1.24 ml·min^{-1}·cm^{-2} under 40% CO_2 and down to 0.27 ml·min^{-1}·cm^{-2} under 100% CO_2. Despite the fact that O_2 fluxes worsen even when protecting BSCF membrane (probably due to surface imperfections letting CO_2 to be in contact with BSCF[18], and/or because O_2-CO_2 competitive adsorption taking place on CGO layer surface), there is an evident positive effect of CGO coating when membrane is exposed to CO_2. The 4-fold improvement in J(O_2) obtained when using pure CO_2 as sweep gas is a remarkable fact that protecting BSCF membranes with 500 nm thick CGO layers by RF-sputtering is a promising way for overcoming the well-known BSCF instability under CO_2-containing environments. The exploitation of this concept can lead the way to the use of highly permeating materials like BSCF in applications where high J(O_2) and chemical and mechanical stability on harsh environments are needed. Nevertheless, optimization is as well needed in order to minimize O_2 permeation drops observed in the protected membrane: improving layer coating and layer composition, thus avoiding the generation of holes, cracks or un-protected areas.

In order to check the microstructure of the membrane after permeation tests, Figure 6 shows the surface of the CGO films on the BSCF bulk membrane and a cross section of film and membrane after permeation. Both CGO and BSCF are dense, and a 300-500 nm CGO film covers the whole surface of the membrane. No high density of defects is observed which ensures the effectiveness of the CGO protection against CO_2.

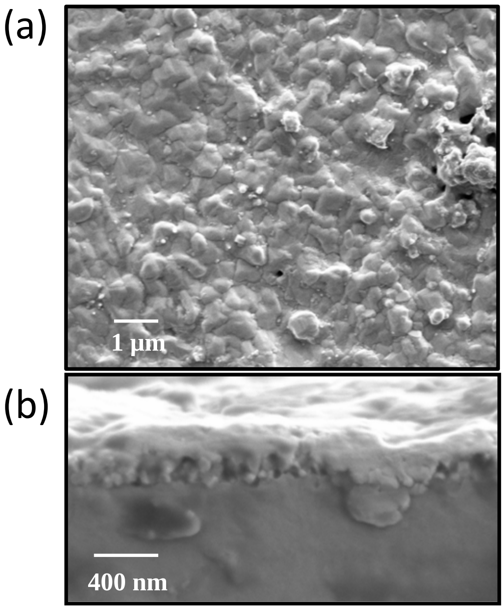

Figure 6: Superficial morphology of the CGO film (a) and cross section image (b) of the CGO film on the BSCF bulk membrane after permeation tests and CO_2 exposure.

Conclusions

CGO thin films protective layers deposited by RF magnetron sputtering were studied and optimized on quartz substrates and then applied on BSCF oxygen permeation membranes. The oxygen permeation of the BSCF is improved by thin CGO layer, with a 4-fold improvement in the oxygen permeation flux when using pure CO_2 as sweep gas at 900 °C. These CGO protective layers are a suitable method for overcoming the well-known BSCF instability under CO_2-containing environments.

Acknowledgements

Funding from the Spanish Government (RTI2018-102161, SEV-2016-0683 and IJCI-2017-34110 grants) and Generalitat Valenciana (PROMETEO/2018/006 grant) is kindly acknowledged. The support of the Servicio de Microscopía Electrónica of the Universitat Politècnica de València is also acknowledged.

Conflicts of interest

There are no conflicts of interest to declare.

Notes and references

1. J. Garcia-Fayos, M. P. Lobera, M. Balaguer and J. M. Serra, *Frontiers in Materials*, 2018, **5**.
2. S. P. S. Badwal and F. T. Ciacchi, *Advanced Materials*, 2001, **13**, 993-+.
3. R.-h. Yuan, Z. He, Y. Zhang, W.-d. Wang, C.-s. Chen, H. Wu and Z.-l. Zhan, *AIChE Journal*, 2016, **62**, 2170-2176.
4. L. Mastropasqua, G. D. Marcoberardino, P. Chiesa and S. Campanari, *Energy Procedia*, 2017, **142**, 1589-1594.
5. J. Sunarso, S. Baumann, J. M. Serra, W. A. Meulenberg, S. Liu, Y. S. Lin and J. C. D. da Costa, *Journal of Membrane Science*, 2008, **320**, 13-41.
6. J. F. Vente, S. McIntosh, W. G. Haije and H. J. M. Bouwmeester, *Journal of Solid State Electrochemistry*, 2006, **10**, 581-588.
7. H. J. M. Bouwmeester, M. W. Den Otter and B. A. Boukamp, *Journal of Solid State Electrochemistry*, 2004, **8**, 599-605.
8. A. Leo, S. Smart, S. Liu and J. C. D. da Costa, *Journal of Membrane Science*, 2011, **368**, 64-68.
9. S. Baumann, J. M. Serra, M. P. Lobera, S. Escolastico, F. Schulze-Kuppers and W. A. Meulenberg, *Journal of Membrane Science*, 2011, **377**, 198-205.
10. L. Almar, H. Störmer, M. Meffert, J. Szász, F. Wankmüller, D. Gerthsen and E. Ivers-Tiffée, *ACS Applied Energy Materials*, 2018, **1**, 1316-1327.
11. J. Xue, L. Chen, Y. Wei and H. Wang, *Chemical Engineering Journal*, 2017, **327**, 202-209.
12. J. Xue, Q. Liao, Y. Wei, Z. Li and H. Wang, *Journal of Membrane Science*, 2013, **443**, 124-130.
13. I. Garcia-Torregrosa, M. P. Lobera, C. Solis, P. Atienzar and J. M. Serra, *Advanced Energy Materials*, 2011, **1**, 618-625.
14. C. Solís, F. Toldra-Reig, M. Balaguer, S. Somacescu, J. Garcia-Fayos, E. Palafox and J. M. Serra, *ChemSusChem*, 2018, **11**, 2818-2827.
15. W. Fang, C. Zhang, F. Steinbach and A. Feldhoff, *Angewandte Chemie International Edition*, 2017, **56**, 7584-7588.
16. M. Balaguer, C. Solis and J. M. Serra, *Journal of Physical Chemistry C*, 2012, **116**, 7975-7982.
17. B. Wei, Z. Lu, X. Q. Huang, J. P. Miao, X. Q. Sha, X. S. Xin and W. H. Su, *Journal of the European Ceramic Society*, 2006, **26**, 2827-2832.
18. M. Schulz, R. Kriegel and A. Kaempfer, *Journal of Membrane Science*, 2011, **378**, 10-17.
19. M. Balaguer, C. Solis and J. M. Serra, *Chemistry of Materials*, 2011, **23**, 2333-2343.
20. H. Luo, K. Efimov, H. Jiang, A. Feldhoff, H. Wang and J. Caro, *Angewandte Chemie International Edition*, 2011, **50**, 759-763.
21. M. Yashima and T. Takizawa, *The Journal of Physical Chemistry C*, 2010, **114**, 2385-2392.
22. M. Mogensen, N. M. Sammes and G. A. Tompsett, *Solid State Ionics*, 2000, **129**, 63-94.
23. M. Mogensen, N. M. Sammes and G. A. Tompsett, *Solid State Ionics*, 2000, **129**, 63-94.
24. W. C. Oliver and G. M. Pharr, *Journal of Materials Research*, 1992, **7**, 1564-1583.
25. Q. Fang and J. Y. Zhang, *Surface & Coatings Technology*, 2002, **151**, 100-104.
26. E. Jud, C. B. Huwiler and L. J. Gauckler, *Journal of the Ceramic Society of Japan*, 2006, **114**, 963-969.
27. Y. J. Kim, Y. Gao, G. S. Herman, S. Thevuthasan, W. Jiang, D. E. McCready and S. A. Chambers, *Journal of Vacuum Science & Technology A*, 1999, **17**, 926-935.
28. A. Rothschild, W. Menesklou, H. L. Tuller and E. Ivers-Tiffee, *Chemistry of Materials*, 2006, **18**, 3651-3659.
29. C. Kleinlogel and L. J. Gauckler, *Solid State Ionics*, 2000, **135**, 567-573.
30. A. Kossoy, Y. Feldman, E. Wachtel, I. Lubomirsky and J. Maier, *Advanced Functional Materials*, 2007, **17**, 2393-2398.

31. I. Lubomirsky, *Solid State Ionics*, 2006, **177**, 1639-1642.
32. N. I. Karageorgakis, A. Heel, J. L. M. Rupp, M. H. Aguirre, T. Graule and L. J. Gauckler, *Advanced Functional Materials*, 2011, **21**, 532-539.
33. J. L. M. Rupp, E. Fabbri, D. Marrocchelli, J. W. Han, D. Chen, E. Traversa, H. L. Tuller and B. Yildiz, *Advanced Functional Materials*, 2014, **24**, 1562-1574.
34. S. Kim and J. Maier, *Journal of the European Ceramic Society*, 2004, **24**, 1919-1923.
35. M. Balaguer, V. B. Vert, L. Navarrete and J. M. Serra, *Journal of Power Sources*, 2013, **223**, 214-220.
36. E. Quarez, K. V. Kravchyk and O. Joubert, *Solid State Ionics*, 2012, **216**, 19-24.
37. M. Arnold, H. Wang and A. Feldhoff, *Journal of Membrane Science*, 2007, **293**, 44-52.
38. M. Czyperek, P. Zapp, H. J. M. Bouwmeester, M. Modigell, K. Ebert, I. Voigt, W. A. Meulenberg, L. Singheiser and D. Stöver, *Journal of Membrane Science*, 2010, **359**, 149-159.
39. J. Yi and M. Schroeder, *Journal of Membrane Science*, 2011, **378**, 163-170.
40. M. Balaguer, J. García-Fayos, C. Solís and J. M. Serra, *Chemistry of Materials*, 2013, **25**, 4986-4993.
41. M. P. Lobera, J. M. Serra, S. P. Foghmoes, M. Søgaard and A. Kaiser, *Journal of Membrane Science*, 2011, **385–386**, 154-161.
42. S. Engels, T. Markus, M. Modigell and L. Singheiser, *Journal of Membrane Science*, 2011, **370**, 58-69.